Ribbon- and Boardlike Nanostructures of Nickel Hydroxide: Synthesis, Characterization, and Electrochemical Properties

Dongning Yang,[†] Rongming Wang,[‡] Maoshuai He,[†] Jin Zhang,*[,†] and Zhongfan Liu*[,†]

Key Laboratory for the Physics and Chemistry of Nanodevices, Centre for Nanoscale Science and Technology, College of Chemistry and Molecular Engineering, and School of Physics, Peking University, Beijing 100871, People's Republic of China

Received: January 6, 2005; In Final Form: February 22, 2005

We report the synthesis, characterization, and electrochemistry properties of ribbon- and boardlike nanostructures of nickel hydroxide, which crystallize in different phases. The ribbonlike nanostructures (nanoribbons) of nickel hydroxide were synthesized by treating amorphous α-$Ni(OH)_2$ with high concentrations of nickel sulfate. These nanoribbons crystallized in a new phase had typical widths of 5−25 nm, thicknesses of 3−9 nm, and lengths of up to a few micrometers. After further treatment in alkali at 60 °C, the nanoribbons converted to boardlike nanostructures (nanoboards), which crystallized in the β-phase with the average length−width−thickness ratio of 20:6:1. The crystal structures, Raman spectra, and electrochemical properties of these nanostructures of nickel hydroxide are described in this paper. For comparison, the amorphous α-$Ni(OH)_2$ has also been investigated. Moreover, the intermediate product between the nanoribbons and the nanoboards displays a unique structure, which implied an interesting transformation process. The nanoribbons with the new phase show some unique features in Raman spectra, two new peaks located at 3534 and 3592 cm^{-1} in the OH stretching region, indicating the new chemical environment of the hydroxyl groups. The nanoboards exhibit the highest specific capacity, which is close to the theoretical capacity of β-$Ni(OH)_2$. It suggests that the boardlike nanostructure is helpful in improving the electrochemical performance of nickel hydroxide. Because of their unique structures and properties, the nanoribbons and nanoboards of nickel hydroxide may give a new perspective for applications in the areas of catalysts and rechargeable batteries.

Introduction

Nickel hydroxide has attracted great interest since it has been widely used as a cathode material in a number of nickel-based rechargeable alkaline batteries (e.g., Ni/Cd, Ni/H_2, Ni/MH, Ni/Fe, and Ni/Zn).[1] Because the performance of such batteries depends on the structural and morphological features of $Ni(OH)_2$, considerable work has been done to prepare and investigate bulky or nanocrystalline $Ni(OH)_2$ with different phases.[2−8]

It has long been known that nickel hydroxide has a hexagonal layered structure with two polymorphs, α and β.[2,9] α-$Ni(OH)_2$ is isostructural with hydrotalcite and consists of stacked $Ni(OH)_{2-x}$ layers intercalated with various anions or water molecules. This phase is hydroxyl deficient and can be formulated as $Ni(OH)_{2-x}(A^{n-})_{x/n}\cdot yH_2O$, where $x = 0.2-0.4$, $y = 0.6-1$, and A = chloride, sulfate, nitrate, carbonate, or other anions,[10] while in the case of β-$Ni(OH)_2$, it has a well-ordered brucite-like structure and does not contain any intercalated species. In addition to the two well-known phases, other modified phases such as α* and β_{bc} (bc = badly crystallized) have also been reported.[11−14] We have recently synthesized nanoribbons of nickel hydroxide, which crystallized in a new phase, quite different from these known phases of $Ni(OH)_2$.[15] Among these phases of nickel hydroxide, β-phase is the classical material used in rechargeable batteries. The β-$Ni(OH)_2$ is usually oxidized to β-NiOOH in a charge process and has a maximum theoretical specific capacity of 289 mAh/g. Because α-$Ni(OH)_2$ can be oxidized to γ-NiOOH and the average oxidation state of nickel in γ-NiOOH is 3.5 or higher, the α-$Ni(OH)_2$ has a superior theoretical specific capacity reaching up to 433 mAh/g.[11,16] However, the pure α-$Ni(OH)_2$ is very unstable in water and alkali and quickly transforms to the β-phase.

Besides crystal structure, morphologies of $Ni(OH)_2$ also have a significant influence on its electrochemical properties.[17−19] It has been found that $Ni(OH)_2$ with a smaller crystalline size exhibits better electrochemical properties.[17,18] Reisner et al. have developed nanostructured β-$Ni(OH)_2$, a mixture of nanofibers and nanoparticles, which was expected to yield at least a 20% improvement in cathode energy content.[19]

With the development of one-dimensional (1D) nanostructures,[20] the synthesis of 1D nanostructured electrode materials holds great technological promise for improving the performance of rechargeable batteries and for fabricating micro- and nanobatteries.[19,21] However, few studies have been focused on the 1D nanostructures of nickel hydroxide.[19,22] Through the hydrothermal process, Kyotani et al. have obtained 1D nanorods of β-$Ni(OH)_2$ within an anodic oxide template.[22] Nevertheless, it is impossible to obtain pure $Ni(OH)_2$ nanorods because of the decomposition of $Ni(OH)_2$ while removing template.

In this work, we report systematically an investigation on the synthesis, characterization, and electrochemistry properties of the nickel hydroxide nanoribbons and nanoboards, which crystallize in different phases. The two forms as well as the

* Corresponding authors. Telephone/Fax: 86-10-6275-7157. E-mail: jinzhang@pku.edu.cn.
[†] College of Chemistry and Molecular Engineering.
[‡] School of Physics.

10.1021/jp050083b CCC: $30.25
Published on Web 03/22/2005

amorphous α-$Ni(OH)_2$ exhibited very dissimilar X-ray diffraction patterns, Raman spectra, and electrochemical properties. Moreover, the transformation from the nanoribbons to nanoboards has also been investigated. Because of the unique structures and properties, these 1D nanostructures of nickel hydroxide may find applications in the catalytic field and the battery industry.

Experimental Section

All of the chemicals were of analytical grade and used without further purification. Distilled water was used throughout. $NiSO_4 \cdot 6H_2O$ and NaOH were all supplied by Beijing Chemical Reagent Co.

Sample Preparation. *Synthesis of Amorphous α-Ni(OH)$_2$ (Sample A).* The sample of amorphous α-$Ni(OH)_2$ was synthesized by mixing 40 mL of 0.8 M NaOH and 160 mL of 0.3 M $NiSO_4$ to form a nickel hydroxide slurry. The slurry was immediately filtered and washed repeatedly with distilled water.

Synthesis of Nanoribbons of Ni(OH)$_2$ (Sample B).[15] The nanoribbons of nickel hydroxide were synthesized from the nickel hydroxide slurry similar to that used to synthesize sample A. The slurry was loaded in a 250 mL Teflon flask, sealed, and heated for 24 h at 100 °C. The product was filtered and washed with large amounts of distilled water.

Synthesis of Nanoboards of Ni(OH)$_2$ (Sample C). The nanoboards of β-$Ni(OH)_2$ were prepared by heating sample B in 0.2−0.5 M NaOH solution for 24−48 h at 60 °C. The final product was collected by filtration and washed with distilled water.

Synthesis of Intermediate Product between the Nanoribbons and the Nanoboards of Ni(OH)$_2$ (Sample D). The experiment process is the same as the procedure for the synthesis of the nanoboards of β-$Ni(OH)_2$, except for the treating time, treating nanoribbons for 3 h at 60 °C.

All four samples were dried at 100 °C in a vacuum.

Characterization. X-ray powder diffraction (XRD) patterns were collected with a Japan Rigaku Dmax/2000 X-ray diffractometer with graphite monochromatized Cu Kα radiation. Low-resolution transmission electron microscopy (TEM) images were obtained using a JEOL JEM 200CX transmission electron microscope operated at 120 kV. High-resolution TEM (HRTEM) images were taken with a Philips TECNAI-F30 transmission electron microscope, using an accelerating voltage of 300 kV. X-ray fluorescence spectroscopy (XRF) images were recorded on a Bruker S4-Explorer X-ray fluorescence spectrometer, using nonmonochromatized Mg KR X-ray as the excitation source, and choosing C 1s (284.60 eV) as the reference line. A Renishaw 1000 micro-Raman system (He−Ne laser excitation wavelength of 632.8 nm, spot size ~1 μm diameter) was used to characterize the samples. For Raman study, the samples were placed directly on the test floor without any further treatment.

Evaluation of Electrochemical Properties. To evaluate the electrochemical properties of the three samples, nickel hydroxide electrodes were prepared as follows. The nickel hydroxide samples (65 wt %) were mixed with nickel powder (26.4 wt %), cobalt oxide powder (7.6 wt %), and carboxymethyl cellulose (CMC) (1 wt %) in water as a binder. The mixtures were stirred to obtain pastes. The nickel foam substrates with a size of 4.0 × 4.0 cm^2 were then filled with the pastes and dried at 100 °C for 6 h. All electrochemical studies were performed in a three-electrode cell with a 6.0 M KOH solution at room temperature. A metal hydride (MH) electrode with a capacity in excess of the nickel hydroxide electrodes was uses as a counter electrode, and a Hg/HgO electrode was used as a reference electrode. The nickel hydroxide electrodes were charged at a rate of 0.3 C for 5 h and discharged at a 0.3 C rate to 1.0 V. Electrochemical measurements were performed using a LAND model BT1-50 battery-test system.

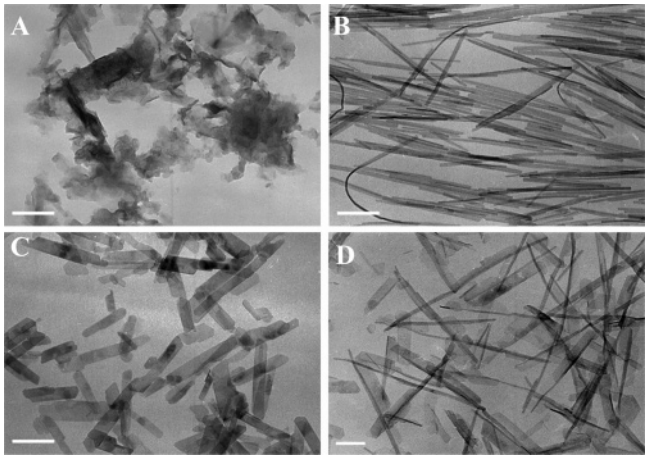

Figure 1. Morphologies of the nickel hydroxide samples revealed by TEM: (A) sample A, (B) sample B, (C) sample C, (D) sample D. Scale bar: 100 nm.

Results and Discussion

Morphology. The morphologies of the samples were characterized by TEM. As shown in Figure 1A, sample A was an amorphous product. The amorphous form is mostly due to obtaining the precipitate in excess nickel sulfate without aging.[9] Figure 1B revealed that sample B consisted almost exclusively of a large number of ribbonlike nanostructures. The nanoribbons had typical lengths of 0.2−2 μm and widths of 5−25 nm. Analysis of a number of nanoribbons with different widths revealed that individual nanoribbons were uniform in width. TEM images from sample C (Figure 1C) showed a mixed morphology consisting mainly of new boardlike nanostructures with a small amount of irregularly contoured nanosheets, which was different from the spherical particles of β-$Ni(OH)_2$ prepared using conventional methods.[23] The typical lengths and widths of the nanoboards were in the ranges of 80−250 and 25−60 nm, respectively. The nanoboards have a small length-to-width ratio, in correspondence with a ribbonlike morphology.

The thicknesses of the nanoribbons and the nanoboards were examined by atomic force microscopy (AFM, Digital Instrument, Nanoscope III, USA) using tapping mode. The thicknesses of the nanoribbons varied from 3 to 9 nm with an average close to 5.5 nm, while the nanoboards had thicknesses ranging from 4 to 9 nm with an average around 6.0 nm. These results suggested that the nanoribbons and the nanoboards were about the same thickness. The combination of AFM and TEM allowed us to obtain the average length−width−thickness ratio of the nanoboards, which was 20:6:1.

Sample D, the intermediate product between the nanoribbons and the nanoboards, showed particular morphologies (Figure 1D). Many nanoribbons are broken down, and some nanoboards are formed. Most of the nanoboards are directly connected to the nanoribbons. This typical morphology is also shown in Figure 4A, which indicates that the nanoribbons provide templates for the formation of the nanoboards.

Composition. The chemical composition of the different phases was determined by XRF, and by chemical and thermogravimetric analyses. The combination of these different experimental techniques allowed us to obtain an approximate formula for each sample. Samples A and B can be represented

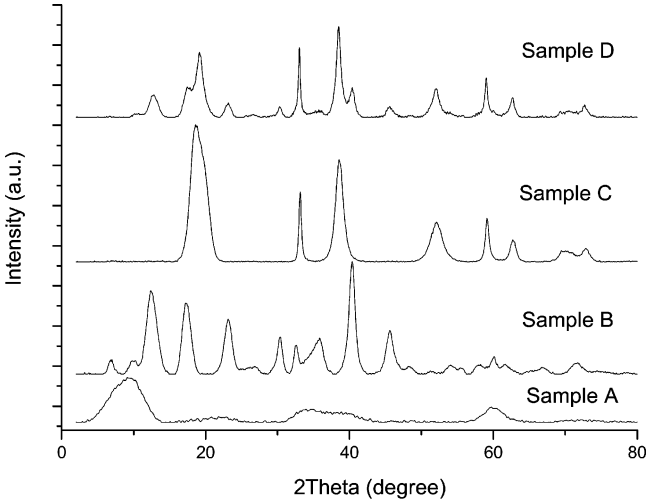

Figure 2. XRD patterns of the nickel hydroxide samples.

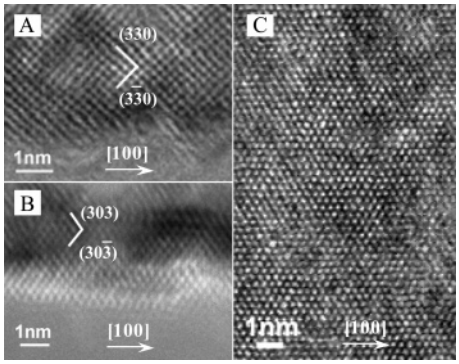

Figure 3. HRTEM images of (A) the wide face of a nanoribbon, (B) the narrow face of another nanoribbon, and (C) the wide face of a nanoboard.

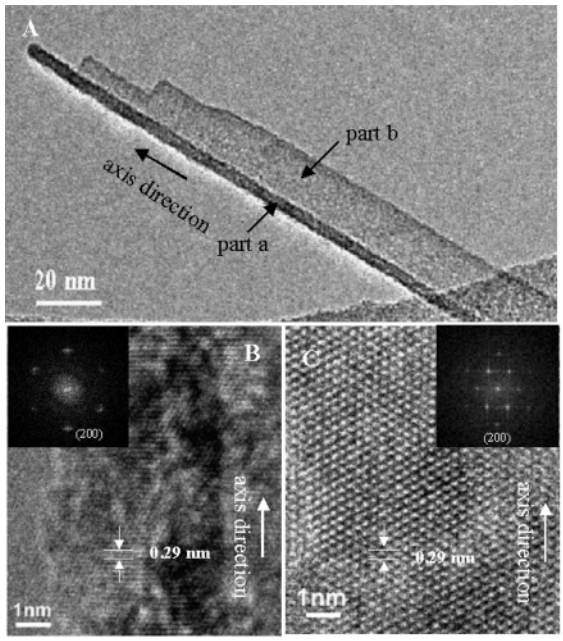

Figure 4. (A) TEM image of a typical intermediate between the nanoribbons and the nanoboards of nickel hydroxide, (B) HRTEM image of the nanoribbon part (part a) of the intermediate, and (C) HRTEM image of the nanoboard part (part b) of the intermediate; the insets are the corresponding FFTs of the images.

by the formulas of $Ni(OH)_{1.62}(SO_4)_{0.19}(H_2O)_{0.24}$ and $Ni(OH)_{1.68}(SO_4)_{0.16}(H_2O)_{0.19}$, respectively. The content of sulfate ions in sample A is slightly more than that in sample B. Sample C has the composition of $Ni(OH)_2$, and the sulfate ions have been completely ejected (corroborating with Raman data present below).

Crystal Structure. The XRD data from the samples were shown in Figure 2. The pattern of Sample B was different from those of the other samples. Neither the position of the peaks nor their relative intensities corresponded to either of the two known phases, α-$Ni(OH)_2$ or β-$Ni(OH)_2$.[10,15,24] After a detailed analysis, it was concluded that this pattern corresponded to a new phase for nickel hydroxide.[15] The peaks in the pattern of sample B were indexed as a monoclinic unit cell, and the lattice parameters were calculated to be $a = 8.74(1)$ Å, $b = 8.60(1)$ Å, $c = 12.58(2)$ Å, and $\beta = 91.2(2)°$ with PowderX.[25] The strongest six peaks (7.15, 5.126, 3.837, 2.940, 2.232, 1.991 Å) could be indexed to (101), ($\bar{1}$02), ($\bar{1}$03), (104), (232), and ($\bar{1}$16) planes, respectively. The broadening of peaks in the XRD patterns shown in Figure 2 might be mainly attributed to structural disorder.[10c]

The XRD measurement shows that sample C possesses hexagonal structure with lattice constants of $a = 3.120(2)$ Å and $c = 4.606(2)$ Å calculated by PowderX,[25] consistent with the standard values for β-$Ni(OH)_2$.[24] The peaks at $d = 4.73$, 2.70, 2.33, 1.74, 1.56, and 1.48 Å correspond to (001), (100), (101), (102), (110), and (111) reflections, respectively.

The XRD curve of sample A shows the typical pattern of an α-phase.[10] The broad asymmetric band in the 2.2−2.7 Å region is the typical structure of turbostratic α-$Ni(OH)_2$.

The XRD results suggest that the amorphous α-$Ni(OH)_2$ could transform to the new phase of nickel hydroxide with ribbonlike nanostructures by heating in high concentrations of nickel sulfate. A high concentration of nickel sulfate is the crucial factor for the synthesis of the nickel hydroxide nanoribbons, as demonstrated in the previous work.[15]

HRTEM images of individual nanoribbons and nanoboards (Figure 3A and B) provide further insight into the morphologies and structure details of these materials. Figure 3A shows an HRTEM image recorded near the edge of a nickel hydroxide nanoribbon along the direction perpendicular to the wide face of the nanoribbon. This image clearly reveals (330) and (3$\bar{3}$0) planes with spacings of 0.202 and 0.203 nm, respectively. The growth direction of the nanoribbon is parallel to the [100] direction, and the wide face of the nanoribbon corresponds to the (001) plane. An HRTEM image taken from the narrow face of another nanoribbon is given in Figure 3B. The spacings of 0.232 and 0.235 nm correspond to the (303) and (30$\bar{3}$) planes, respectively, indicating that the narrow face is the (010) plane. The observation of Figure 3B further confirms that the as-synthesized nanoribbons are single crystals with a preferential [100] growth direction along their long axes. The results from Figure 3A and B are coherent with the cell parameters calculated from XRD.

Figure 3C exhibits the HRTEM image taken from the wide face of a nanoboard. This image reveals that the nanoboard was formed with a single crystalline structure and growth direction along [100]. The lattice in the image is arranged in a hexagon, and the intervals of the closest points are measured to be 0.30 nm, which corresponds to the lattice parameter a of β-$Ni(OH)_2$.

Transformation from Nanoribbons to Nanoboards. To investigate the transformation from nanoribbons to nanoboards, TEM and HRTEM images of a typical intermediate were taken (Figure 4A−C). The typical intermediate (shown in Figure 4A) is composed of a nanoribbon part (part a) and a nanoboard part (part b). The fact that the distance between atomic planes (indicated by lines in Figure 4B) is identical to that of (100)

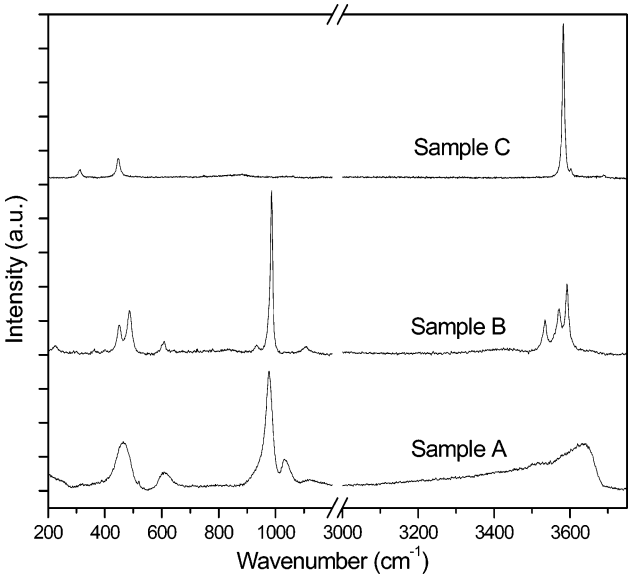

Figure 5. Raman spectra of samples A−C.

lattice planes of β-Ni(OH)$_2$ suggests that the surface of the nanoribbon part is the (001) facet of β-Ni(OH)$_2$. The inset shows the fast Fourier transform (FFT) of the digital HRTEM image. The HRTEM image recorded on the nanoboard part (Figure 4C) exhibits a hexagonal lattice, which indicated the surface of the nanoboard part is also the (001) plane of β-Ni(OH)$_2$. The XRD pattern of sample D displays peaks of two phases: the new phase and β-phase. The low intensity of the peaks corresponding to the new phase implied that sample D contains some remaining nanoribbons, whose crystal structure does not change. The unique structure of the intermediate product apparently indicates that in the transformation process the nanoribbons not only change their crystal structure, but also provide templates for the growth of β-phase nanoboards.

Raman Spectra. Raman spectroscopy was performed to obtain further structural information of the samples. Samples A−C (Figure 5A and B) exhibit very dissimilar Raman spectra because of their different morphology and structural characteristics.

The spectrum of sample A displays two characteristic bands of α-Ni(OH)$_2$,[27,28] a broad band centered around 3640 cm^{-1} and an intense band at 465 cm^{-1}. The broad band between 3300 and 3680 cm^{-1} is related to the stretching vibration of the hydroxyl groups. The 465 cm^{-1} band can be attributed to a Ni−O(H) stretching mode.[28−30] The spectrum of sample A also shows some additional features, a complex system of bands located in the 600−1100 cm^{-1} range. The bands at 609, 977, and 1032 cm^{-1} can be attributed to some adsorbed sulfate species.[30,31]

The spectrum of sample B shows some unique features. Three strong lines at 3534, 3572, and 3592 cm^{-1} are observed in the OH stretching region. The 3572 cm^{-1} line is close to that observed for β-phase samples,[27,28,32] which can be assigned to the symmetric stretching of the hydroxide groups. The appearance of new lines at 3534 and 3592 cm^{-1} could be explained by the presence of these hydrogen atoms in a different environment. The line at 3534 cm^{-1} is most likely due to the stretching mode of the hydroxyl groups involved in hydrogen bonding. The hydrogen bonding comes from absorbed H_2O and from hydroxyl groups interacting with adsorbed species, particularly H_2O.[30,31] The 3592 cm^{-1} line is associated with the stretching of free hydroxyl groups near the surface of the crystallites.[17] Because the intensity of this line is proportional to the surface area of the crystallites,[17] high intensity of this line suggests that sample B has a large extended surface area. In the metal−oxygen stretching region (400−600 cm^{-1}), the band at 451 cm^{-1} can be attributed to the stretching vibration of Ni−OH,[17,30,33] and the 488 cm^{-1} band is most likely due to Ni−O vibration.[33] In addition, the bands correlated with sulfate anions have been observed at 609 and 986 cm^{-1}.

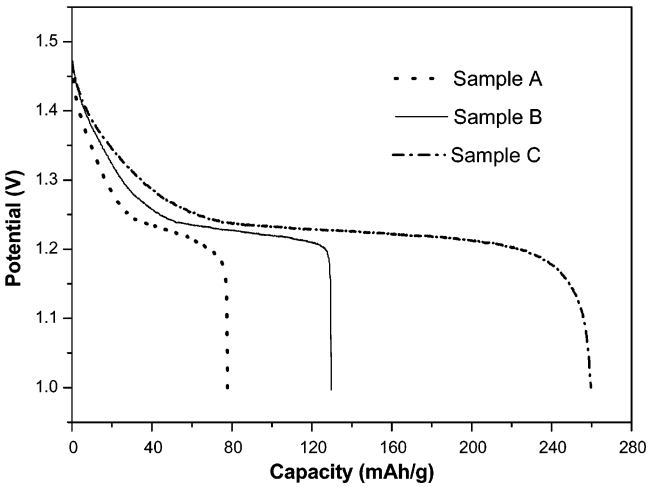

Figure 6. Discharge curves of the nickel hydroxide electrodes.

Sample C shows the typical β-Ni(OH)$_2$ spectrum.[6,17,27] The peaks at 311 and 447 cm^{-1} can be ascribed to the E-type vibration of the Ni−OH lattice and the Ni−OH stretch, respectively. The 3583 cm^{-1} peak is assigned to the symmetric stretch of the hydroxyl groups. In addition, the lines associated with sulfate species have not been detected, indicating that the sulfate anions are completely removed.

Electrochemical Properties. Figure 6 displays the discharge curves of the three as-prepared nickel hydroxide electrodes after activation of four charge−discharge cycles. The electrodes differed in the electrochemical capacity, 78 mAh/g for the electrode containing sample A, 130 mAh/g for the electrode containing sample B, and 260 mAh/g for the electrode containing sample C. Sample C exhibits the highest specific capacity, which is close to the theoretical capacity of β-nickel hydroxide. This result suggests that the boardlike nanostructure is helpful for improving the electrochemical performance of nickel hydroxide. In contrast, sample A with the phase has a capacity that is lower than its theoretical capacity. According to the investigation of other researchers, the low capacity of α-Ni(OH)$_2$ may be caused by the structure transformation and the capacity fading in a strong alkaline medium.[34] The transformation of the crystal structure would result in crystallite breaking and loss of contact of the active materials with the conductive substrate. It was found that the new phase would easily convert to β-Ni(OH)$_2$ in 5 M NaOH solution at room temperature. Most likely due to the new phase fast fading in a strong alkaline medium, sample B with the new phase exhibits the low specific capacity, which is 67% higher than that of the amorphous α-Ni(OH)$_2$. To stabilize the α-phase in strong alkali, some metal ions such as aluminum were used to partially substitute nickel ions in the α-phase.[3,16,34c] The aluminum stabilized α-phase can provide a higher specific capacity than the β-phase.[3] This implies that when stabilized in strong alkali, this new phase with ribbonlike nanostructures may also exhibit excellent performance as well as aluminum stabilized α-nickel hydroxide.

Conclusions

In the present study, we report systematically an investigation on the synthesis, characterization, and electrochemistry proper-

ties of the nickel hydroxide nanoribbons and nanoboards. The nanoribbons of nickel hydroxide were synthesized by heating amorphous α-$Ni(OH)_2$ in high concentrations of nickel sulfate. Through the further treatment in alkali at 60 °C, the nanoribbons would convert to the β-phase of nickel hydroxide with boardlike nanostructures. The nanoribbons and nanoboards of nickel hydroxide as well as the amorphous α-$Ni(OH)_2$ exhibited quite different XRD patterns, Raman spectra, and electrochemical properties. The unique structure of the intermediate product between the nanoribbons and the nanoboards indicates that the nanoribbons not only change their crystal structure, but also provide templates for the growth of β-phase nanoboards in the transformation process. The nanoribbons with the new phase showed some unique features in Raman spectra, two new peaks located at 3534 and 3592 cm^{-1} in the OH stretching region, indicating the new chemical environment of the hydroxyl groups. The nanoboards exhibit the highest specific capacity, which is close to the theoretical capacity of β-$Ni(OH)_2$. It indicates that the boardlike nanostructure is helpful in improving the electrochemical performance of nickel hydroxide, while in the case of the nanoribbons, the specific capacity of these nanostructures is only 130 mAh/g. Considering the stability in strong alkali, the new phase of nickel hydroxide with a ribbonlike nanostructure still could be improved with regards to the specific capacity.

Acknowledgment. This work was supported by the National Natural Science Foundation of China (NSFC 90206023), and the Ministry of Science and Technology of China (2001CB6105, 2002CB613505). We would like to express our gratitude to Mr. Jiang Changying for his generous help with the electrochemical measurements.

References and Notes

(1) (a) Ovshinsky, S. R.; Fetcenko, M. A.; Ross, J. *Science* **1993**, *260*, 176. (b) Oshitani, M.; Yufu, H.; Tskashima, K.; Tsuji, S.; Matsumaru, Y. *J. Electrochem. Soc.* **1989**, *136*, 1590.

(2) Oliva, P.; Leonardi, J.; Laurent, J. F.; Delmas, C.; Braconnier, J. J.; Figlarz, M.; Fievet, F.; De Guibert, A. *J. Power Sources* **1982**, *8*, 229.

(3) (a) Ehlsissen, K. T.; Delahaye-Vidal, A.; Genin, P.; Figlarz, M.; Willmann, P. *J. Mater. Chem.* **1993**, *3*, 883. (b) Kamath, P. V.; Dixit, M.; Indira, L.; Shukla, A. K.; Kumar, V. G.; Munichandraiah, N. *J. Electrochem. Soc.* **1994**, *141*, 2956. (c) Hu, W. K.; Noreus, D. *Chem. Mater.* **2003**, *15*, 974.

(4) Soler-Illia, G. J. D. A.; Jobbagy, M.; Regazzoni, A. E.; Blesa, M. A. *Chem. Mater.* **1999**, *11*, 3140.

(5) Delahaye-Vidal, A.; Beaudoin, B.; Sac-Epee, N.; Tekaia-Elhsissen, K.; Audemer, A.; Figlarz, M. *Solid State Ionics* **1996**, *84*, 239.

(6) Bernard, M. C.; Kaddam, M.; Takenouti, H.; Bernard, P.; Senyarich, S. *J. Electrochem. Soc.* **1996**, *143*, 2447.

(7) Jeevanandam, P.; Koltypin, Y.; Gedanken, A. *Nano Lett.* **2001**, *1*, 263.

(8) Chen, J.; Bradhurst, D. H.; Dou, S. X.; Liu, H. K. *J. Electrochem. Soc.* **1999**, *146*, 3606.

(9) Oswald, H. R.; Asper, R. In *Preparation and Crystal Growth of Materials with Layered Structure*; Lieth, R. M. A., Ed.; D. Reidel: Dordrecht, The Netherlands, 1977.

(10) (a) Kamath, P. V.; Therese, G. H. A.; Gopalakrishnan, J. *J. Solid State Chem.* **1997**, *128*, 38. (b) Rajamathi, M.; Kamath, P. V. *J. Power Sources* **1998**, *70*, 118. (c) Ramesh, T. N.; Jayashree, R. S.; Kamath, P. V. *Clays Clay Miner.* **2003**, *51*, 570.

(11) Faure, C.; Delmas, C.; Fouassier, M. *J. Power Sources* **1991**, *35*, 279.

(12) Braconnier, J. J.; Delmas, C.; Fouassier, C.; Figlarz, M.; Beaudouin, B.; Hagenmuller, P. *Rev. Chim. Miner.* **1984**, *21*, 496.

(13) Rajamathi, M.; Subbanna, G. N.; Kamath, P. V. *J. Mater. Chem.* **1997**, *7*, 2293.

(14) Rajamathi, M.; Kamath, P. V.; Seshadri, R. *J. Mater. Chem.* **2000**, *10*, 503.

(15) Yang, D. N.; Wang, R. M.; Zhang, J.; Liu, Z. F. *J. Phys. Chem. B* **2004**, *108*, 7531.

(16) (a) Buss, D. H.; Bauer, J.; Diembeck, W.; Glemser, O. *J. Chem. Soc., Chem. Commun.* **1985**, 81. (b) Corrigan, D. A.; Knight, S. L. *J. Electrochem. Soc.* **1989**, *136*, 613.

(17) Bernard, M. C.; Cortes, R.; Keddam, M.; Takenouti, H.; Bernard, P.; Senyarich, S. *J. Power Sources* **1996**, *63*, 247.

(18) Watanabe, K.; Kikuoka, T. *J. Appl. Electrochem.* **1995**, *25*, 219.

(19) Reisner, D. E.; Salkind, A. J.; Strutt, P. R.; Xiao, T. D. *J. Power Sources* **1997**, *65*, 231.

(20) (a) Hu, J. T.; Odom, T. W.; Lieber, C. M. *Acc. Chem. Res.* **1999**, *32*, 435. (b) Xia, Y. N.; Yang, P. D.; Sun, Y. G.; Wu, Y. Y.; Mayers, B.; Gates, B.; Yin, Y. D.; Kim, F.; Yan, H. Q. *Adv. Mater.* **2003**, *15*, 353. (c) Pan, Z. W.; Dai, Z. R.; Wang, Z. L. *Science* **2001**, *291*, 1947. (d) Shi, W. S.; Peng, H. Y.; Wang, N.; Li, C. P.; Xu, L.; Lee, C. S.; Kalish, R.; Lee, S. T. *J. Am. Chem. Soc.* **2001**, *123*, 11095.

(21) (a) Che, G. L.; Lakshmi, B. B.; Fisher, E. R.; Martin, C. R. *Nature* **1998**, *393*, 346. (b) Dominko, R.; Arcon, D.; Mrzel, A.; Zorko, A.; Cevc, P.; Venturini, P.; Gaberscek, M.; Remskar, M.; Mihailovic, D. *Adv. Mater.* **2002**, *14*, 1531. (c) Dewan, C.; Teeters, D. *J. Power Sources* **2003**, *119*, 310.

(22) Matsui, K.; Kyotani, T.; Tomita, A. *Adv. Mater.* **2002**, *14*, 1216.

(23) Yang, C. C. *Int. J. Hydrogen Energy* **2002**, *27*, 1071.

(24) Joint Committee on Powder Diffraction Standards (JCPDS), file No. 14-117; International Center for Diffraction Data: Swathmore, PA.

(25) Dong, C. *J. Appl. Crystallogr.* **1999**, *32*, 838.

(26) Scherrer, P. *Gott. Nachr.* **1918**, *2*, 98.

(27) Cornilsen, B. C.; Karjala, P. J.; Loyselle, P. L. *J. Power Sources* **1988**, *22*, 351.

(28) Kostecki, R.; McLarnon, F. *J. Electrochem. Soc.* **1997**, *144*, 485.

(29) Densilvestro, J.; Corrigan, D. A.; Weaver, M. J. *J. Phys. Chem.* **1986**, *90*, 6408.

(30) Deabate, S.; Fourgeot, F.; Henn, F. *J. Power Sources* **2000**, *87*, 125.

(31) Frost, R. L.; Weier, M. L.; Kloprogge, J. T. *J. Raman Spectrosc.* **2003**, *34*, 760.

(32) Johnston, C.; Graves, R. R. *Appl. Spectrosc.* **1990**, *44*, 105.

(33) Lo, Y. L.; Hwang, B. J. *Langmuir* **1998**, *14*, 944.

(34) (a) Bode, H.; Dehmelt, K.; Witte, J. *Electrochim. Acta* **1966**, *11*, 1079. (b) Barnard, R.; Randell, C. F.; Tye, F. L. *J. Appl. Electrochem.* **1980**, *10*, 109. (c) Dai, J.; Li, S. F. Y.; Xia, T. D.; Wang, D. M.; Reisner, D. E. *J. Power Sources* **2000**, *89*, 40.